Entropy Engineering in I-V-VI_2 clan: A paradigm to bestow suppression of phase transition in the entire operating temperature regime

Ranita Basu [a,b,*], U. Sandhya Shenoy [c], Ankita Pathak [a,b], Shweta Singh [b,d], P. Jha[a,b], D. Krishna Bhat [e], Hirakendu Basu[b,d], and Ajay Singh [a,b]

[a]*Technical Physics Division, Bhabha Atomic Research Centre, Mumbai 400085, India.*
[b]*Homi Bhabha National Institute, Training School Complex, Anushaktinagar, Mumbai 400094, India.*
[c]*Department of Materials Science and Engineering, Institute of Engineering and Technology, Srinivas University, Mukka 574146, Mangalore, Karnataka, India*
[d]*Analytical Chemistry Division, Bhabha Atomic Research Centre, Mumbai 400085, India.*
[e]*Department of Chemistry, National Institute of Technology Karnataka, Surathkal, Srinivasnagar 575025, Mangalore, Karnataka, India*
[*]*Corresponding author: ranitapaul@gmail.com ; ranitab@barc.gov.in; Tel.: (+91)2225593217*

1.0.Experimental details:

1.1 Synthesis: The multinary solid solution of (AgBiSeS)1-x(PbSe)x were synthesized via vacuum melting method where stoichiometric amount of high purity Ag, Bi, Pb, Se and S were premixed and filled in quartz tubes. After evacuation at 10^{-5} mbar, the tubes were flame-sealed and gradually heated at the rate of 35K/hr to 723 K. Subsequently, the tube was heated at the rate of 100 K/hr to 1123 K, soaked for 6 hrs at this temperature and finally water quenched to room temperature. The ingot so obtained were hand ground in an agate mortar pestle to have fine powder. The fine powder was subsequently filled in a 10 mm graphite die set, and sintered using vacuum hot-press technique at 823 K with an axial compressive stress of 50 MPa for 30 minutes. The resultant dense pellet shows a theoretical density > 96%. These pellets were eventually sealed in an evacuated quartz tube and annealed at 823 K for 7 days for thermodynamically stable microstructure.

1.2. Characterization: X-Ray diffraction, electron microscopy, Raman spectroscopy and X-ray photoelectron spectroscopy:

The pellets, before and after sintering, were characterized by the X-ray diffraction technique using a Proto AXRD Benchtop Powder diffractometer, under ambient conditions diffractometer in the Bragg–Brentano geometry, using CuKa radiation (l = 1.5418 Å). The diffraction peaks in Fig. 1 (a) is broad owing to the fact that the reported room temperature XRD pattern is for the powder of the pellets after sintering. Since the strength of the pellets after sintering was high, so the pellets were crushed to form powder using ball-milling for short duration at moderate rotation per minute (300 rpm). The broad diffraction peak can be attributed to the reduction in grain size due to ball-milling. Further, a scanning electron microscope (SEM, M/s. JEOL IT300 operated at 15 kV) was used to study the morphology and

the attached EDS analyzer (M/s. EDAX-Octane) was used for elemental analysis and mapping. The specimens for transmission electron microscopy (JEOL JEM2100F) were created by dispersing the specimen powder onto a copper grid. The phonon vibration modes in the samples were studied using a LabRAM-1 micro/macro-Raman spectrometer (Horiba Jobin Yvon, Bensheim, Germany) with a He–Ne laser (λ = 633 nm) as the excitation source. The Raman signals were analyzed using a Peltier-cooled CCD detector for multichannel detection. X-Ray photoelectron spectroscopy (XPS) measurements were carried out using a Mg-Ka (1253.6 eV) source and a DESA-150 electron analyzer (Staib Instruments, Germany). The binding energy scale was calibrated to the Au-4f7/2 line of 84.0 eV. Data were collected for X-rays with an incidence angle of ~54.7^{o} relative to the analyser. The other parameters are a step size of 38 meV and a dwell time of 100 ms. The scanning time was 15–20 min depending on the number of scans. For high resolution, XPS spectra were obtained by averaging 15 scans. While fitting the XPS data with two or more peaks the constraint of full-width at half-maximum (FWHM) for each peak was applied. The XPS peaks were fitted using a combination of Gaussian and Lorentzian distributions. Baseline corrections of the data were done using a Shirley background.

1.3. Electrical transport properties:

The obtained hot-pressed pellets were cut into bars with dimensions of 10mm* 3 mm* 3 mm for simultaneous measurement of the Seebeck coefficient and electrical conductivity using a M/s. Linseis LSR-3 instrument under a helium atmosphere from room temperature to 823 K. No hysteresis was seen in heating and cooling cycles. Electrical properties measured for different slices cut from the same pellets were similar, corroborating the homogeneity of the samples. The uncertainty of the Seebeck coefficient and electrical conductivity measurements is ~3%.

1.4. Thermal transport properties:.

Highly dense hot-pressed pellets of diameter 10 mm were polished for thermal diffusivity measurements. The samples were coated with a thin layer of graphite to minimize errors from the emissivity of the material. The thermal conductivity was calculated from $\kappa_{total} = D * C_P * \rho$, where the thermal diffusivity coefficient (D) was measured by the laser flash diffusivity method using a Linseis LFA-1000 instrument. In this work D was directly Measured by laser flash technique (usingLinseismakeLFA-1000). Cp was estimated by comparative method using high density graphite disc as a standard sample. All thermoelectric

properties were measuredfrom300 to823 K. The uncertainty of α and ρ measurement are about ~5% and ~3% respectively, while for κ measurement the uncertainty is about ~6%.
Unless otherwise mentioned, all the properties described in this study were measured perpendicular to the sintering pressure direction, although no directional anisotropy effects were perceived in the charge transport properties.

1.5. Computational Details:

First principles density functional theory methods implemented in the Quantum ESPRESSO code were used to perform electronic structure calculations Fully relativistic ultrasoft pseudopotentials were used to replace the potential of the ionic core and valence electrons were taken into consideration for the calculation. Inclusion of relativistic pseudopotentials was essential to capture the spin– orbit coupling interaction. The generalized gradient approximation was used for the exchange correlation energy functional with Perdew, Burke and Erzenhoff (PBE) parametrization. A $(\sqrt{2}\times\sqrt{2}\times2)a_o$ supercell of PbSe was constructed. Pristine PbSe and AgBiSeS alloyed compositions were simulated using the same supercell. 50 Ry cut off for energy density and 400 Ry cut off for charge density was set for the calculations. Γ-X-M-Γ-Z-R-A-Z path was used for the determination of band structure along the high symmetry points.

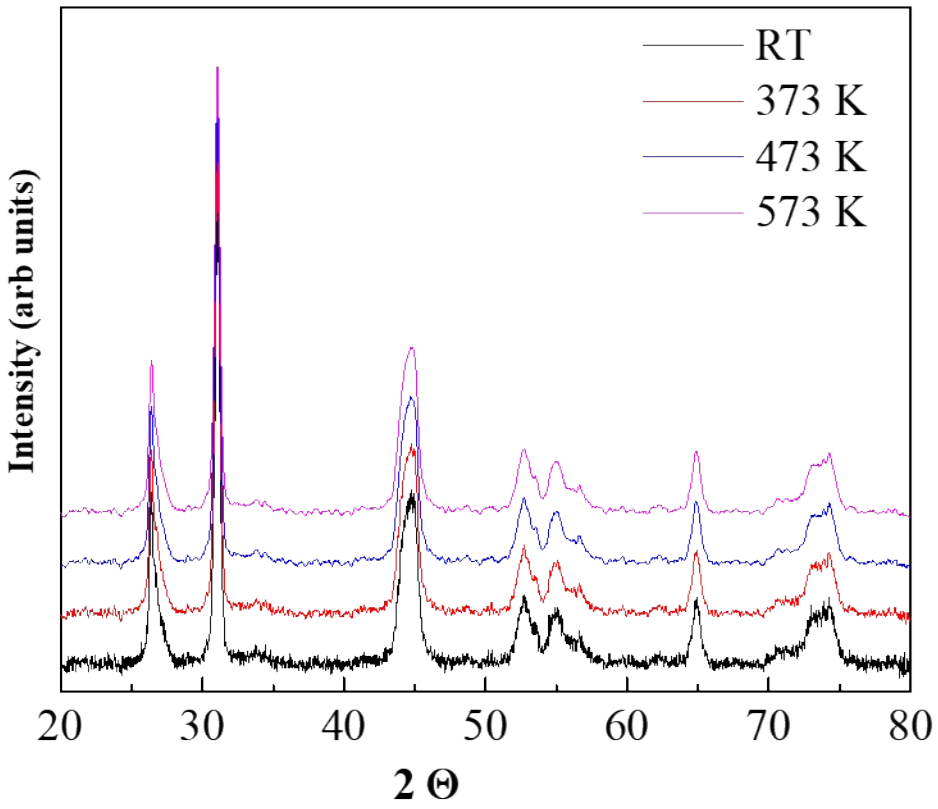

Fig. S1. HT-XRD of $(AgBiSeS)_{0.5}(PbSe)_{0.5}$ to ascertain thermal stability of the entropy engineered alloy.

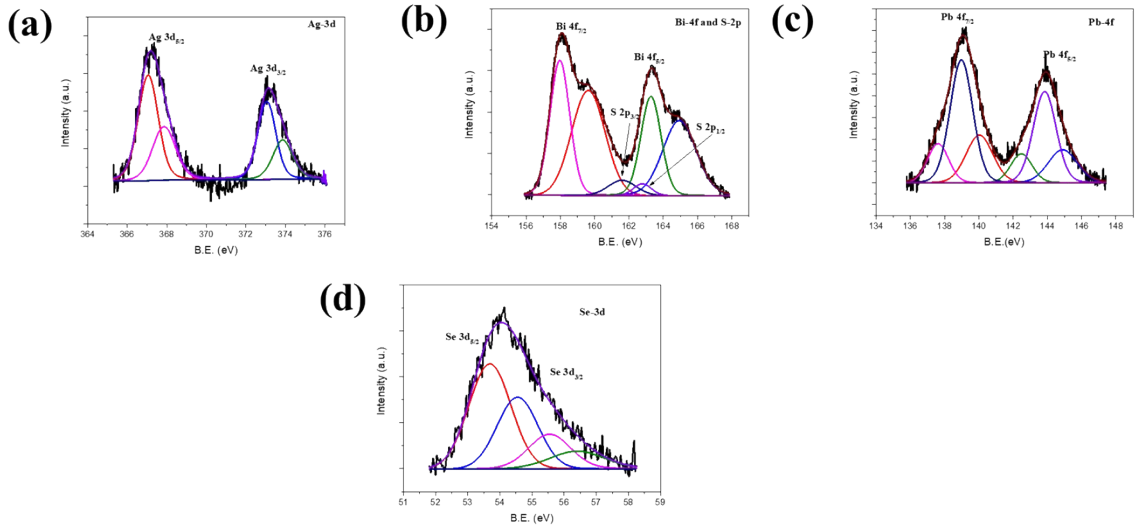

Fig. S2. (a) X-ray photoelectron spectra : (a) Ag-3d; (b) Bi-4f and S-2p; (c) Pb-4f and (d) Se-3d.

As illustrated in Figure S2a, two strong peaks of Ag 3d that emerge around 367.9 eV and 373.9 eV is ascribed to Ag $3d_{5/2}$ and Ag $3d_{3/2}$, respectively, which correspond to the +1 Ag oxidation state. The peaks of Bi 4f are split into $4f_{7/2}$ (157.97eV) and $4f_{5/2}$ (163.28 eV) in Figure S2b, indicating the +3 state for Bi in the final product. Two more peaks corresponding to Bi indicates two different chemical environment of Bi. The peaks of S 2p are split into $S2p_{3/2}$ (161.6 eV) and $S2p_{1/2}$ (162.8 eV) in Figure S2b, indicating S^{2-} in the final product. Figure S2c exhibits two peaks with binding energies at 137.6 eV and 142.5 eV, which are associated with Pb $4f_{7/2}$ and $4f_{5/2}$, respectively, and are consistent with the +2 state. Furthermore, the spin-orbit peaks at $3d_{5/2}$ (53.7 eV) and $3d_{3/2}$ (54.5 eV) are both assigned to the -2 state (Figure S2d).

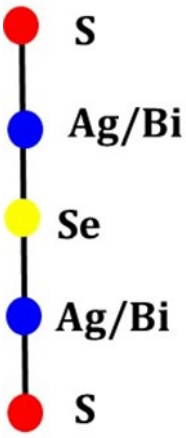

Fig. S3. Schematic representation of the arrangement of the atoms in AgBiSeS.

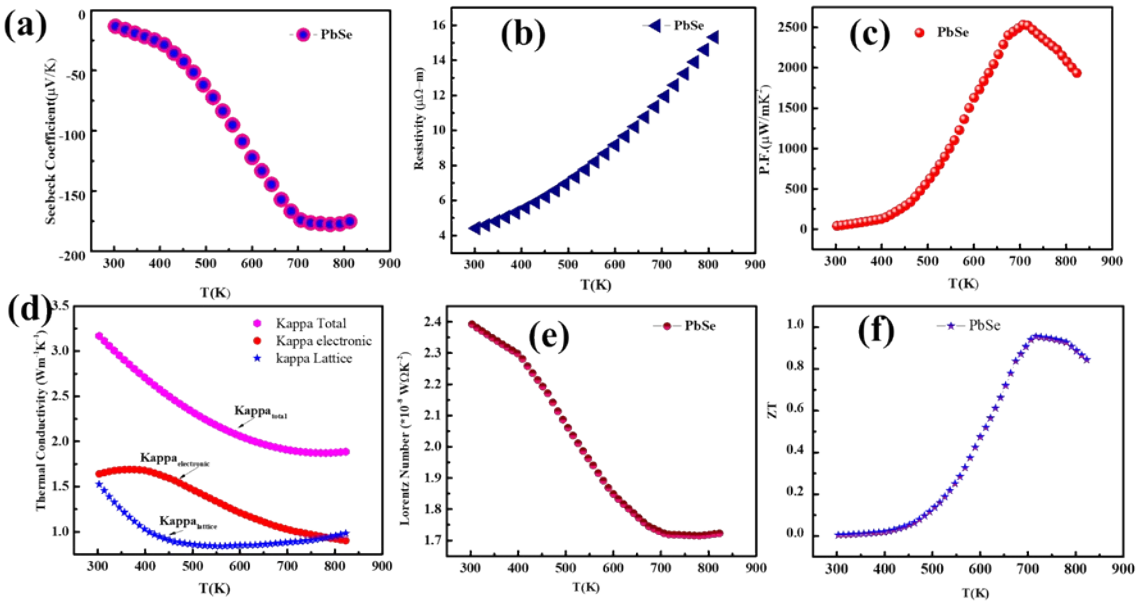

Fig. S4. Electronic and thermal transport properties of PbSe

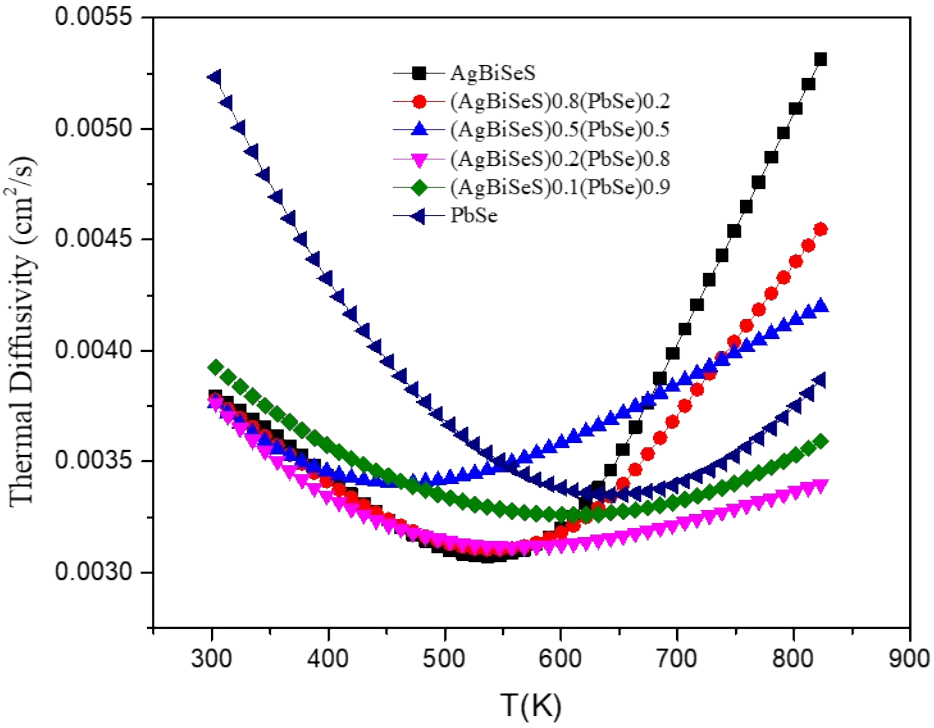

Fig. S5. Temperature dependent thermal diffusivity plot of pristine AgBiSeS, PbSe and $(AgBiSeS)_{1-x}(PbSe)_x$

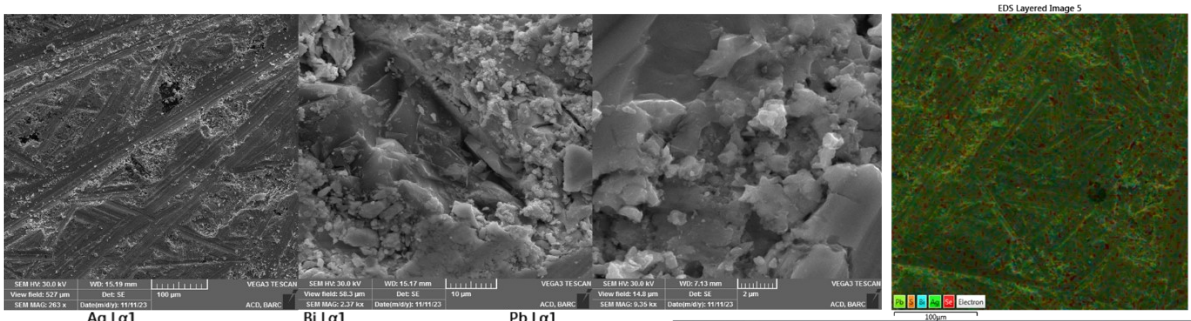

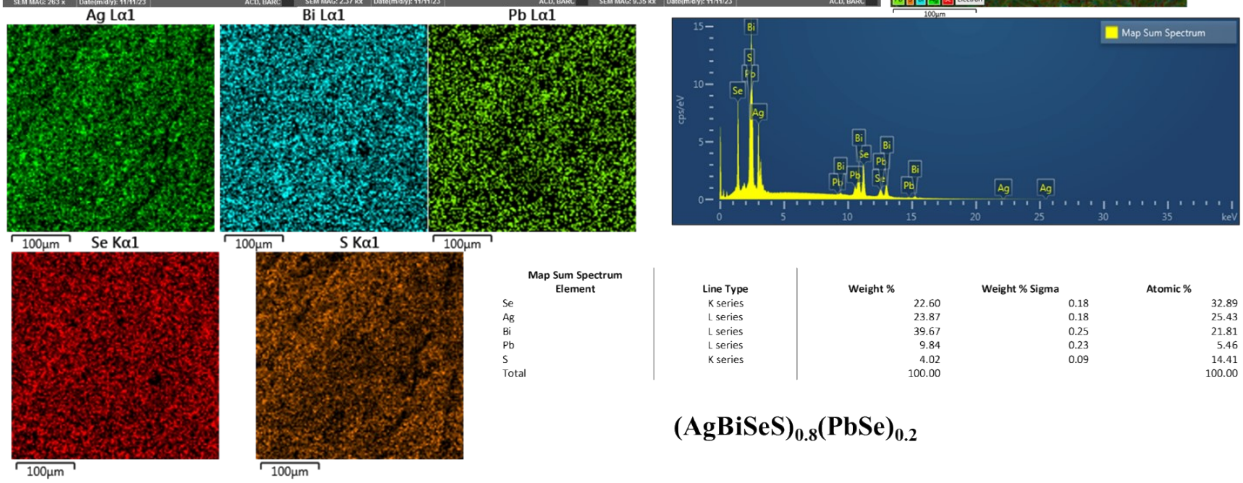

Map Sum Spectrum Element	Line Type	Weight %	Weight % Sigma	Atomic %
Se	K series	22.60	0.18	32.89
Ag	L series	23.87	0.18	25.43
Bi	L series	39.67	0.25	21.81
Pb	L series	9.84	0.23	5.46
S	K series	4.02	0.09	14.41
Total		100.00		100.00

$(AgBiSeS)_{0.8}(PbSe)_{0.2}$

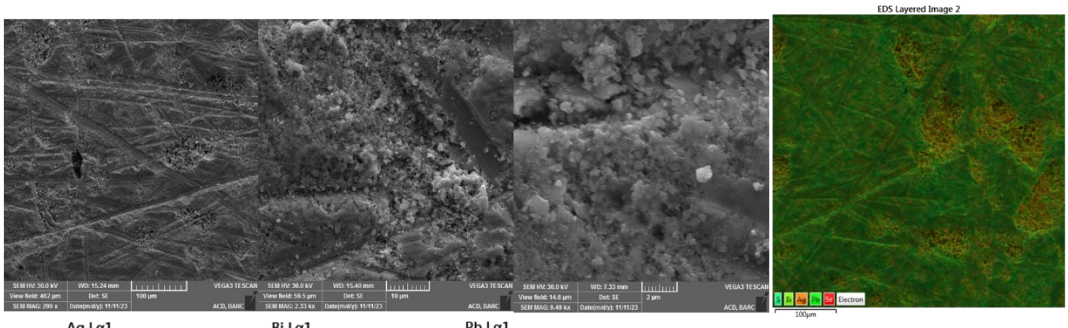

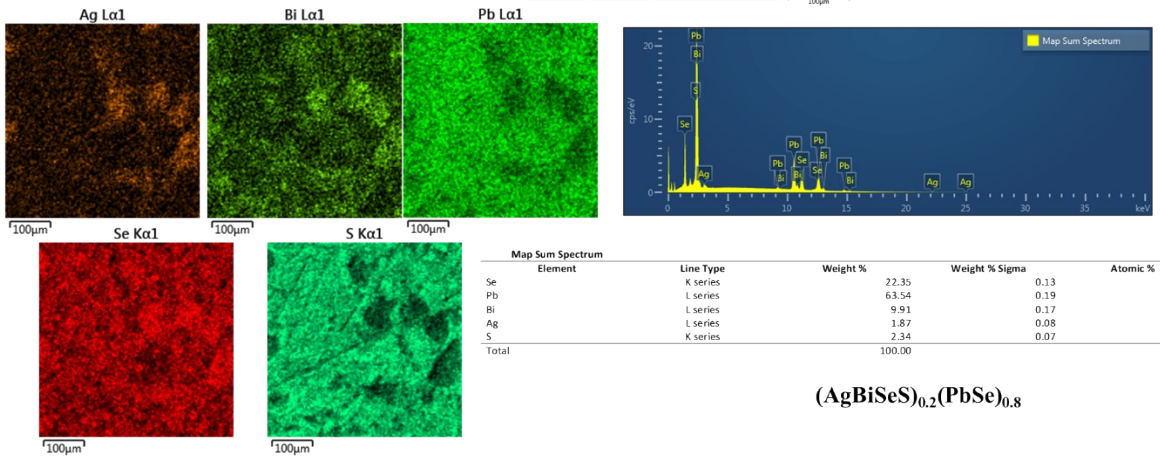

Map Sum Spectrum Element	Line Type	Weight %	Weight % Sigma	Atomic %
Se	K series	22.35	0.13	38.92
Pb	L series	63.54	0.19	42.17
Bi	L series	9.91	0.17	6.52
Ag	L series	1.87	0.08	2.38
S	K series	2.34	0.07	10.02
Total		100.00		100.00

$(AgBiSeS)_{0.2}(PbSe)_{0.8}$

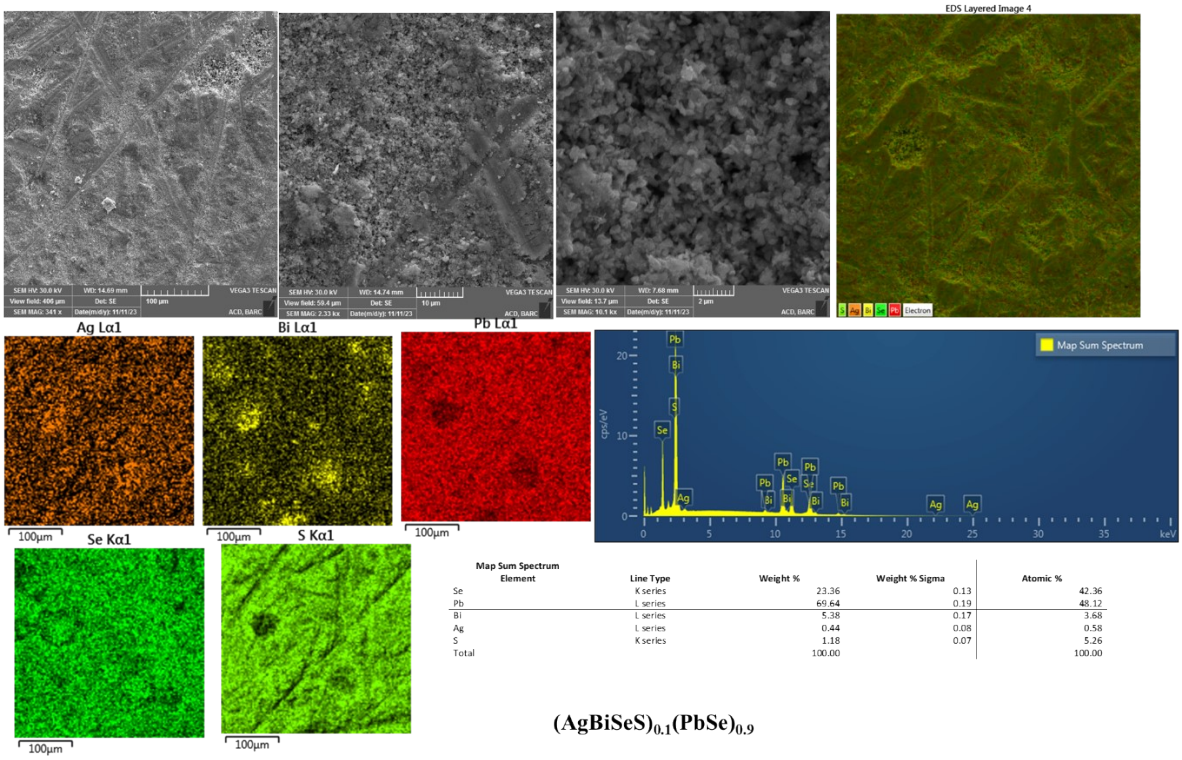

Fig. S6. SEM micrographs and EDS mapping of the solid solution of $(AgBiSeS)_{1-x}(PbSe)_x$.

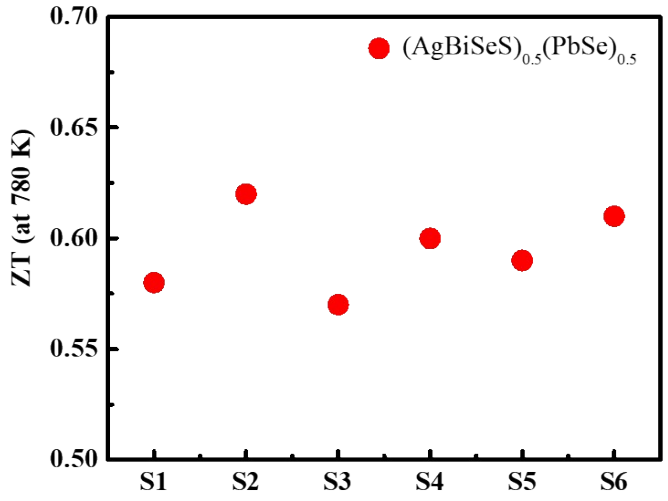

Fig. S7. Repeatibility and reproducibility data of $(AgBiSeS)_{0.5}(PbSe)_{0.5}$.